
QUASI-MONOLITHIC GRAPH NEURAL NETWORK FOR FLUID-STRUCTURE INTERACTION

Rui Gao, Rajeev K. Jaiman
Department of Mechanical Engineering
University of British Columbia
Vancouver, Canada
{garrygao, rjaiman}@mail.ubc.ca

ABSTRACT

Using convolutional neural networks, deep learning-based reduced-order models have demonstrated great potential in accelerating the simulations of coupled fluid-structure systems for downstream optimization and control tasks. However, these networks have to operate on a uniform Cartesian grid due to the inherent restriction of convolutions, leading to difficulties in extracting fine physical details along a fluid-structure interface without excessive computational burden. In this work, we present a quasi-monolithic graph neural network framework for the reduced-order modelling of fluid-structure interaction systems. With the aid of an arbitrary Lagrangian-Eulerian formulation, the mesh and fluid states are evolved temporally with two sub-networks. The movement of the mesh is reduced to the evolution of several coefficients via proper orthogonal decomposition, and these coefficients are propagated through time via a multi-layer perceptron. A graph neural network is employed to predict the evolution of the fluid state based on the state of the whole system. The structural state is implicitly modelled by the movement of the mesh on the fluid-structure boundary; hence it makes the proposed data-driven methodology quasi-monolithic. The effectiveness of the proposed quasi-monolithic graph neural network architecture is assessed on a prototypical fluid-structure system of the flow around an elastically-mounted cylinder. We use the full-order flow snapshots and displacements as target physical data to learn and infer coupled fluid-structure dynamics. The proposed framework tracks the interface description and provides the state predictions during roll-out with acceptable accuracy. We also directly extract the lift and drag forces from the predicted fluid and mesh states, in contrast to existing convolution-based architectures. The proposed reduced-order model via graph neural network has implications for the development of physics-based digital twins concerning moving boundaries and fluid-structure interactions.

1 Introduction

Accurate and efficient predictions and control of the spatial-temporal dynamics of fluid-structure systems are essential in various engineering disciplines. The coupling between fluid and structure can lead to complex dynamical effects such as vortex-induced vibrations and flutter/galloping [1]. Owing to the highly nonlinear and multiscale characteristics of fluid-structure coupling, state-of-the-art computational fluid dynamics (CFD) and finite element analysis (FEA) tools based on the solution of partial differential equations are considered for engineering analysis and design. While high-fidelity CFD/FEA simulations can provide accurate prediction, the high computational cost of these simulations limits their applications for downstream design optimization and control tasks. High-fidelity CFD/FEA simulations can serve the role of a data generator for data-driven predictions, with efficient design iterations or active control of coupled fluid-structure systems. This work is motivated by the need to make coupled fluid-structure simulations efficient for the digital twin technology, whereby multi-query analysis, optimization and control are required.

This limitation of high-fidelity modelling based on partial differential equations has inspired the development of the so-called data-driven reduced-order modeling (ROM) techniques. By constructing low-dimensional models, ROM techniques have the potential to address the limitations of high-fidelity CFD/FEA models for efficient multi-query analysis, optimization and control tasks. Such data-driven models can be used in an offline-online manner, whereby

the models can be trained to learn a low-dimensional representation of the system from the high-dimensional physical data in the offline stage, and provide efficient predictions during the online stage. Numerous data-driven techniques have been developed for low-dimensional modelling and predictive offline-online applications. Popular methods like proper orthogonal decomposition (POD) [2, 3] and dynamic mode decomposition (DMD) [4], as well as their variants (e.g., [5, 6, 7]), are usually based on the projection into a linear subspace. However, these methods encounter difficulty when applied to scenarios with high Reynolds numbers and convection-dominated problems, whereas one needs a significantly large number of linear subspaces to achieve a satisfactory approximation.

In the last decade, deep neural networks have been explored as alternatives to the aforementioned techniques. Autoencoders, as a non-linear extension of POD, have been shown to have significant advantages over POD in the compression of data [8]. Combined with convolution, which supplies the inductive bias of locality and translational equivariance, the convolutional encoder-propagator-decoder architecture have been adopted in many applications, including flow over fixed bodies in both 2D [9, 10, 11, 12] and 3D [13] scenarios, fluid-structure interactions [14, 15], under-water noise propagation [16], and many more. Leveraging the computational power of modern graphical processing units (GPU), the computational times needed for these convolutional neural networks are usually reduced to the level of milliseconds per step, which are orders of magnitude faster than the traditional full-order CFD simulations.

While convolutional neural networks have achieved numerous successes, they have inherent limitations and pose challenges in dealing with fluid-structure boundaries. As convolutions have to be performed on a uniform Cartesian grid, the resolution of the grid on different regions within the simulation domain has to maintain similar resolutions. Considering the flow past a bluff body as an example, the region near the body’s surface is resolved by a grid of the same density as the far field. This means that one must either introduce a significant number of grids in a far-field region that does not feature much physics, or tolerate a relatively low resolution near the body’s surface. The former choice of maintaining a dense grid throughout the bulk and interface requires substantially more computational resources. As a result, the balance usually aligns with the latter, inevitably leading to the loss of fine physical details and the difficulty in extracting important physical statistics like lift and drag coefficients. Despite many efforts to mitigate this issue, by forming a hybrid model with traditional machine learning techniques such as proper orthogonal decomposition [17, 18], interpolation & projection schemes [14], or special mesh design [19], a completely satisfactory solution is not yet available.

Graph neural networks, recently introduced as a geometric deep learning framework, have the ability to address this difficulty, although existing applications are mostly restricted to fluid systems with fixed boundaries. As its name suggests, graph neural networks operate on graphs, which can be intuitively converted from any mesh, meaning that one can control the resolution of the different parts of the simulation domain using the strategies adopted in CFD. As a result, GNNs can maintain a significantly better resolution for important regions within the domain with the same mesh size compared with CNNs. With this clear advantage over CNN, graph neural networks are recently introduced for modeling fluid flow. Applications include flow around fixed bodies like cylinder or airfoil [20, 21], reacting flows [22], flow field super-resolution [23], flow field completion [24], etc. Additional techniques and designs like on-the-fly graph adaptation [20], multi-graph with different level of fineness [21, 25], rotational equivariance [21], quadrature integration-based loss [26], and polynomial processors [22] are also combined with the graph neural networks to further boost their performance.

While these works have demonstrated the potential of graph neural networks for various fluid flow applications, no study exists for the application to fully-coupled fluid-structure systems. Notably, Pfaff et al. [20] simulated the dynamics of flags in their work, but the graph is limited to the flag itself, and the fluid flow surrounding the flag is not simulated. Li et al. [27] simulated the flow flushing around a free-moving rigid box within a container. However, both the flow and the box are discretized into large particles, and therefore losing the fine physical details. Most existing GNN-based works on fluid flow modelling, to the best of the authors’ knowledge, only focus on applications with fixed, rigid body and/or domain boundaries.

In this work, we target to fill this gap in the literature by modelling fluid-structure systems via a graph neural network. Adopting the arbitrary Lagrangian-Eulerian formulation, we propose a quasi-monolithic GNN framework for modelling fluid-structure systems. A GNN sub-network is employed to predict the evolution of the fluid state based on the state of the whole fluid-structure system. Mesh and solid movements are first projected to a lower dimension by POD, and then propagated through time by a multi-layer perceptron sub-network. The solid-state is implicitly modelled by the movement of the mesh on the fluid-solid boundary. The framework is applied to a prototypical fluid-structure problem of an elastically-mounted cylinder case, and is demonstrated to generate accurate roll-out predictions. More importantly, accurate lift and drag force predictions can be directly extracted from the predicted system state by simply integrating the Cauchy stress tensor at the surface of the moving solid body, which is difficult for existing convolution-based frameworks.

This article is organized as follows. In Section 2, we describe the full-order FSI system and the individual components such as proper orthogonal decomposition, multi-layer perceptron and graph neural net for our proposed reduced-order methodology. Section 3 presents a novel quasi-monolithic GNN framework by combining the components. Detailed setup and the results of the experiments on a prototypical fluid-structure interaction problem of an elastically-mounted cylinder system undergoing vortex-induced vibration are covered in Section 4. We conclude the work in Section 5.

2 Computational methodology: Review

Before presenting our quasi-monolithic methodology, we first provide a review of full-order and reduced-order representations of the fluid-structure system. Subsequently, we will introduce the individual components that will be assembled into a complete framework in Sec. 3.

2.1 Full-order system

We briefly summarize the full-order system comprising the Eulerian fluid and the Lagrangian structure, together with the traction and velocity continuity conditions at the fluid-structure interface. Under the arbitrary Lagrangian-Eulerian (ALE) framework, the coupled system between isothermal incompressible viscous fluid flow and an irrotational elastically-mounted rigid body can be modelled as

$$\rho^f \frac{\partial \mathbf{u}^f}{\partial t} + \rho^f (\mathbf{u}^f - \mathbf{w}) \cdot \nabla \mathbf{u}^f = \nabla \cdot \boldsymbol{\sigma}^f + \mathbf{b}^f \quad \text{on } \Omega^f, \quad (1a)$$

$$\nabla \cdot \mathbf{u}^f = 0 \quad \text{on } \Omega^f, \quad (1b)$$

$$\mathbf{m}^s \frac{\partial \mathbf{u}^s}{\partial t} + \mathbf{c}^s \mathbf{u}^s + \mathbf{k}^s (\boldsymbol{\varphi}^s(t) - \boldsymbol{\varphi}^s(0)) = \mathbf{F}^s + \mathbf{b}^s \quad \text{on } \Omega^s, \quad (1c)$$

with boundary conditions on the surface of the rigid body

$$\mathbf{u}^f(t) = \mathbf{u}^s(t) \quad \text{on } \Gamma^{fs}, \quad (2a)$$

$$\mathbf{F}^s(t) = - \int_{\Gamma^{fs}(t)} \boldsymbol{\sigma}^f \cdot \mathbf{n} d\Gamma. \quad (2b)$$

The superscripts $(\cdot)^f$ and $(\cdot)^s$ denote the state parameters for fluid and solid respectively. The fluid, mesh velocity and body force are denoted by \mathbf{u}^f , \mathbf{w} and \mathbf{b}^f respectively within the fluid domain Ω^f , while $\boldsymbol{\varphi}^s$, \mathbf{u}^s , \mathbf{F}^s and \mathbf{b}^s denote the displacement, the velocity, the traction force and the body force for the solid body Ω^s , respectively. The mass, damping, and stiffness matrices for the rigid body are denoted by \mathbf{m}^s , \mathbf{c}^s and \mathbf{k}^s respectively, while ρ^f is the fluid density. At the solid-fluid interface Γ^{fs} , \mathbf{n} denotes the unit outward normal vector. Assuming Newtonian fluid, the Cauchy stress tensor is written as

$$\boldsymbol{\sigma}^f = -p^f \mathbf{I} + \mu^f (\nabla \mathbf{u}^f + (\nabla \mathbf{u}^f)^T), \quad (3)$$

in which p^f denotes the pressure, and μ^f denotes the viscosity of the fluid. We solve the coupled differential equations using the Petrov–Galerkin finite element and the semi-discrete time stepping [1]. For the stable and robust coupling of the fluid–structure interaction, we utilize the nonlinear partitioned staggered procedure [28].

2.2 Reduced-order model

With regard to the reduced-order modelling, the governing Eqs. (1) and (2) can be re-written in the abstract dynamical form

$$\frac{d\mathbf{q}}{dt} = \tilde{\mathbf{F}}(\mathbf{q}), \quad (4)$$

where \mathbf{q} denotes the state of the FSI system. In the present study, the state of the system includes the fluid state, which comprises the velocity $\mathbf{u}^f = (u_x^f, u_y^f)$ and the pressure p^f , as well as the solid state, which involves two degrees of freedom for the translational motion of the rigid body. In Eq. (4), the right hand side term $\tilde{\mathbf{F}}$ represents an underlying dynamic model for the fluid-structure system described in Eqs. 1-3. If we discretize the system with a certain fixed time step δt , then Eq. 4 can be rewritten following forward Euler time integration:

$$\mathbf{q}(t_{n+1}) - \mathbf{q}(t_n) = \delta \mathbf{q} = \mathbf{F}(\mathbf{q}(t_n)), \quad (5)$$

in which $\mathbf{q}(t_n)$ denotes the system state at time step t_n , and \mathbf{F} is the full-order system state update function in the discretized time domain.

With reduced-order modelling, one aims to construct an approximation $\hat{\mathbf{F}}$ to the full-order function \mathbf{F}

$$\mathbf{F}(\mathbf{q}(t_n)) = \mathbf{q}(t_{n+1}) - \mathbf{q}(t_n) \approx \delta \hat{\mathbf{q}} = \hat{\mathbf{F}}(\mathbf{q}(t_n), \theta), \quad (6)$$

in which θ denotes the parameters of the reduced-order model $\hat{\mathbf{F}}$. These parameters are calculated, tuned or trained to minimize the approximation error between the reduced-order model $\hat{\mathbf{F}}$ and the full-order model \mathbf{F}

$$\theta = \arg_{\theta} \min(E[\mathbf{F} - \hat{\mathbf{F}}(\theta)]), \quad (7)$$

in which E denotes the expectation operator, which can vary for different approaches such as projection-based model reduction, system identification or machine learning. For example, proper orthogonal decomposition as a projection-based model reduction minimizes the mean-squared error, i.e., $E[\mathbf{F} - \hat{\mathbf{F}}(\theta)] = \|\mathbf{F} - \hat{\mathbf{F}}(\theta)\|_2$, where $\|\cdot\|_2$ denotes an Euclidean norm. In this work, we construct a fully data-driven reduced-order model $\hat{\mathbf{F}}$ with three components: proper orthogonal decomposition, multi-layer perceptron, and graph neural network. These building blocks will be introduced in the remaining parts of this section, and assembled into a complete framework in Sec. 3.

2.3 Proper orthogonal decomposition

As will be discussed later in Sec. 3.1, we choose to use the arbitrary Lagrangian-Eulerian formulation for the proposed quasi-monolithic GNN framework, which features mesh movements over time. This movement is inherently low-rank, and therefore suitable for a linear projection-based reduction. We employ Proper orthogonal decomposition (POD) for this purpose. Particularly, we use the spatial variant [3] of POD. Given a data matrix \mathbf{X} in which each column contains the mesh displacements at a certain time step, a singular value decomposition can be performed,

$$\mathbf{X} = \mathbf{U}\mathbf{\Sigma}\mathbf{V}^T. \quad (8)$$

Each column of the left unitary matrix \mathbf{U} is called a mode. Suppose the singular values on the diagonal of matrix $\mathbf{\Sigma}$ are in decreasing order. In that case, the left-most vectors within the matrix \mathbf{U} are the modes capturing the most variance in the data. For a low-rank system, a reduced-order model can be constructed by projecting the data onto the first l modes,

$$\mathbf{C}^{(1:l)} = (\mathbf{U}^{(1:l)})^T \mathbf{X}, \quad (9a)$$

$$\hat{\mathbf{X}} = \mathbf{U}^{(1:l)} \mathbf{C}^{(1:l)}, \quad (9b)$$

where $\mathbf{U}^{(1:l)}$ denotes the matrix \mathbf{U} truncated to its left-most l columns (i.e., retaining the first l modes), the coefficient matrix $\mathbf{C}^{(1:l)}$ corresponds to the projected weight of the data on each of the modes, and $\hat{\mathbf{X}}$ denotes the reduced-order approximation of \mathbf{X} using the first few modes. The temporal evolution of the system is then reduced using the evolution of the mode 1 through l coefficients over time.

2.4 Multi-layer perceptron

Multi-layer perceptron (MLP), or alternatively called feedforward neural network, is one of the simplest modern neural networks. For an input vector \mathbf{z} , a multi-layer perceptron with $n_l - 1$ hidden layers can be written as

$$f(\mathbf{z}) = f_{n_l} \circ f_{n_l-1} \circ f_{n_l-2} \circ \cdots \circ f_2 \circ f_1(\mathbf{z}), \quad (10)$$

in which \circ denotes function composition. Each layer f_i is defined as

$$f_i(\mathbf{z}) = \begin{cases} \sigma_i(\mathbf{W}_i \mathbf{z} + \mathbf{b}_i) & i = 1, 2, \dots, n_l - 1 \\ \mathbf{W}_i \mathbf{z} + \mathbf{b}_i & i = n_l \end{cases} \quad (11)$$

where $\mathbf{W}_i \mathbf{z} + \mathbf{b}_i$ is a linear transformation of the input vector \mathbf{z} . The weight matrix \mathbf{W}_i does not have to be a square matrix, i.e., the linear transformation can project the input into a higher or lower dimension matrix. The number of rows in the weight matrix \mathbf{W}_i is called the layer width, and the non-linear function σ_i is usually called the activation function. In this work, multi-layer perceptrons are employed to temporally evolve the POD coefficients of the mesh movements, and are also used as the encoders, decoders, as well as processors for the graph neural network, introduced next in Sec. 2.5.

2.5 Graph neural network

Graph neural networks, as discussed in the introduction, have demonstrated their advantage over convolution-based neural networks in modeling fluid systems, and therefore also utilized in this work. Specifically, we adopt the variant of the message-passing graph neural network proposed by Battaglia et al. [29]. This network architecture has been

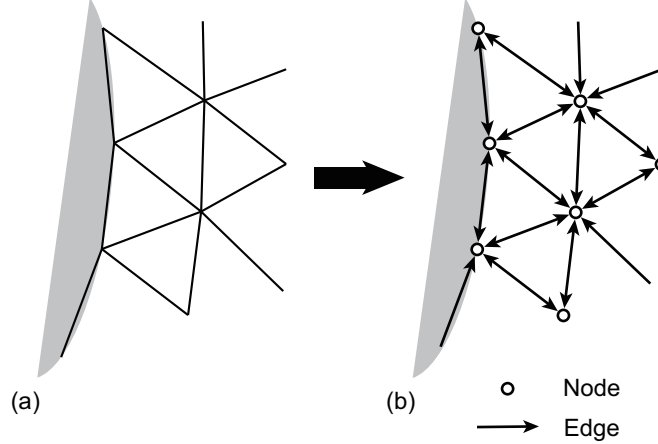


Figure 1: An illustration to transform an unstructured mesh to the corresponding graph: (a) triangular mesh near the solid-fluid boundary, (b) equivalent graph representation. Each vertex in the mesh is converted to a node, while each link between two vertices in the mesh is converted to two directed edges. The direction of each edge is marked by an arrow. System states attached to the mesh are also converted and re-attached to the nodes and edges as their respective feature vectors.

applied to various fluid flow cases [20, 21, 22] and performed well. The network includes three steps: Encoding, message-passing, and decoding. Given a graph converted from a mesh following the illustration in Fig. 1, along with the feature vectors attached to its nodes \mathcal{V} and edges \mathcal{E} , the encoder step can be written as

$$\mathbf{v}_i \leftarrow g^v(\mathbf{v}_i), \quad (12a)$$

$$\mathbf{e}_{ij} \leftarrow g^e(\mathbf{e}_{ij}), \quad (12b)$$

in which \mathbf{v}_i is the feature vector attached to node i , \mathbf{e}_{ij} is the feature vector attached to the directed edge pointing from node i to node j , and g^v and g^e are the node and edge encoders respectively. The left arrow \leftarrow updates the parameter on its left-hand side by its right-hand side value.

The encoded nodes and edges then proceed through a series of message-passing layers, with each layer consisting of an edge update step and a node update step, plotted in Fig. 2. Using the information from each edge itself and the two nodes it connects, the edge update step can be written as

$$\mathbf{e}'_{ij} = \phi^e(\mathbf{e}_{ij}, \mathbf{v}_i, \mathbf{v}_j). \quad (13a)$$

In the subsequent node update step, each node is updated using the information from the node itself and the aggregated information from all the edges pointing to it:

$$\mathbf{v}'_i = \phi^v(\mathbf{v}_i, \text{AGG}_j \mathbf{e}'_{ji}). \quad (13b)$$

The aggregation function AGG is chosen to be the mean function in this work. Note that the edge and node processors ϕ^e and ϕ^v are not necessarily shared for different message-passing layers. The outputs at the end of the message-passing layers are decoded to generate the final outputs. In this work, only outputs on nodes are needed, and therefore only a node decoder h^v is required:

$$\mathbf{v}''_i \leftarrow h^v(\mathbf{v}'_i). \quad (14)$$

With forward Euler time discretization described in Eq. 5, the output nodes \mathbf{v}''_i at each time step will be added to the corresponding entries of the input to serve as the input of the next time step. Further details will be presented in Sec. 3.2, after the discussion of the formulation that governs the proposed quasi-monolithic GNN framework.

3 Quasi-monolithic graph neural network

In this section, we construct the quasi-monolithic GNN framework for FSI systems using the components introduced in Sec. 2. Under the arbitrary Lagrangian-Eulerian formulation, the framework contains two sub-networks: a GNN for the temporally propagating fluid state, and an MLP to evolve the mesh state that is projected to a low dimension via POD. A schematic of the data flow during temporal roll-out is shown in Fig. 3. In the remaining parts of this section, we will first discuss the choice of formulation and then describe the setups of the two sub-networks.

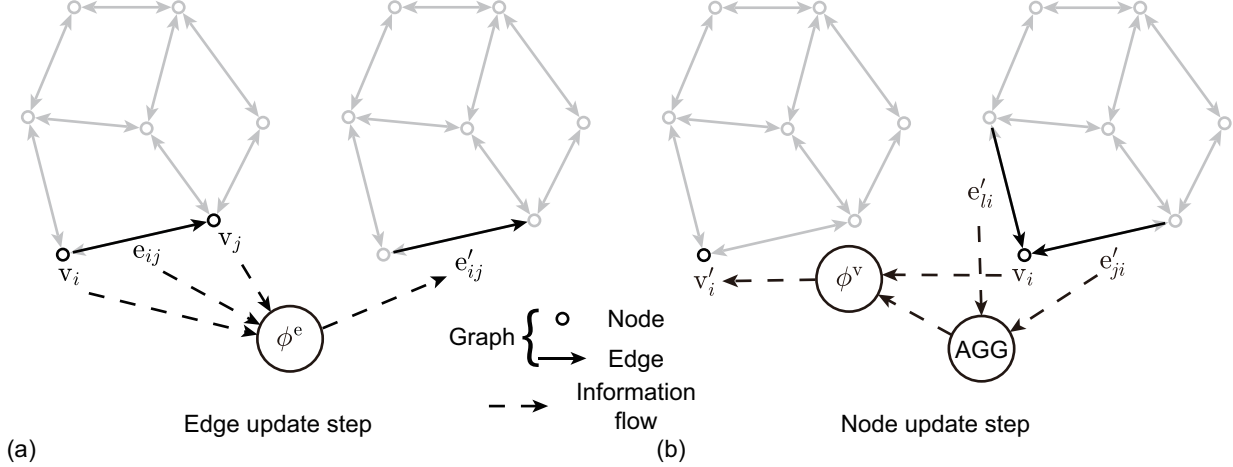


Figure 2: Schematic of the edge and node update steps within each message-passing layer of graph neural network: (a) edge update step, and (b) node update step. In the edge update step, the feature vector v_i attached to node i , the feature vector v_j attached to node j , as well as the feature vector e_{ij} attached to the edge connecting the two nodes, are processed by the edge processor ϕ^e to generate the updated edge feature vector e'_{ij} . In the node update step, the previously updated feature vectors of all the edges connecting to node i are first aggregated through function AGG, and then processed along with the node feature vector v_i by the node processor ϕ^v to generate the updated node feature vector v'_i . The parts of the graph shown in semi-transparent colour are not used within the update steps for the edge feature e_{ij} in (a) and the node feature v_i in (b).

3.1 Choice of formulation, node and edge features

Similar to full-order CFD simulations, the formulation used for the framework has to be chosen first. Since the Reynolds number of the fluid flow is not very low, a fully Lagrangian formulation is not preferable. What is left is the choice between fully Eulerian and arbitrary Lagrangian-Eulerian formulations. For fully-Eulerian formulation, as the solid body is moving within the domain, on-the-fly graph adaptation would be preferable to help maintain a relatively small mesh and graph size. However, numerical experiments by Pfaff et al. [20] showed that the adaptive step for the graph could cost significantly more computational time than running the neural network itself for one step. We therefore choose to use the ALE formulation for the present framework, which features mesh movement according to the movement of the solid body, while the expensive graph adaptation is not necessary.

With the formulation determined, the next step is to convert the mesh to a graph, and re-attach the flow data on the mesh to the nodes and edges of the converted graph. As mentioned in Sec. 2.5, we convert the mesh to graph following the illustration in Fig. 1. The relative location information between the vertices within the mesh are attached to the edges, following Pfaff et al. [20],

$$e_{ij} = [x_i - x_j, y_i - y_j, \sqrt{(x_i - x_j)^2 + (y_i - y_j)^2}], \quad (15)$$

where (x_i, y_i) denotes the spatial location of the vertex corresponding to node i .

The displacement of the mesh from its initial location, however, has to be attached to the nodes because it would be difficult to recover the correct location of the nodes during prediction roll-out if this information is attached to the edges. The fluid state parameters u_x, u_y, p , as well as the border information γ are also attached to the nodes. We drop the superscript $(\cdot)^f$ in the remaining parts of the paper for brevity. The full node feature vector is, therefore

$$v_i = [u_{x,i}, u_{y,i}, p_i, \delta x_i, \delta y_i, \gamma_i], \quad (16)$$

where $u_{x,i}$ and $u_{y,i}$ denote the two velocity components of the flow corresponding to the node i , p_i is the pressure, δx_i and δy_i denote the displacement of the vertex corresponding to node i from its location on the input mesh, and the border information γ_i are encoded in a one-hot manner, which is similar to the work of Pfaff et al. [20].

3.2 GNN for temporal propagation of flow state

We apply the GNN described in Sec. 2.5 for the temporal propagation of the fluid state. Following Eq. 5, we use the network to predict the difference between neighboring temporal steps. With the input node and edge features at time

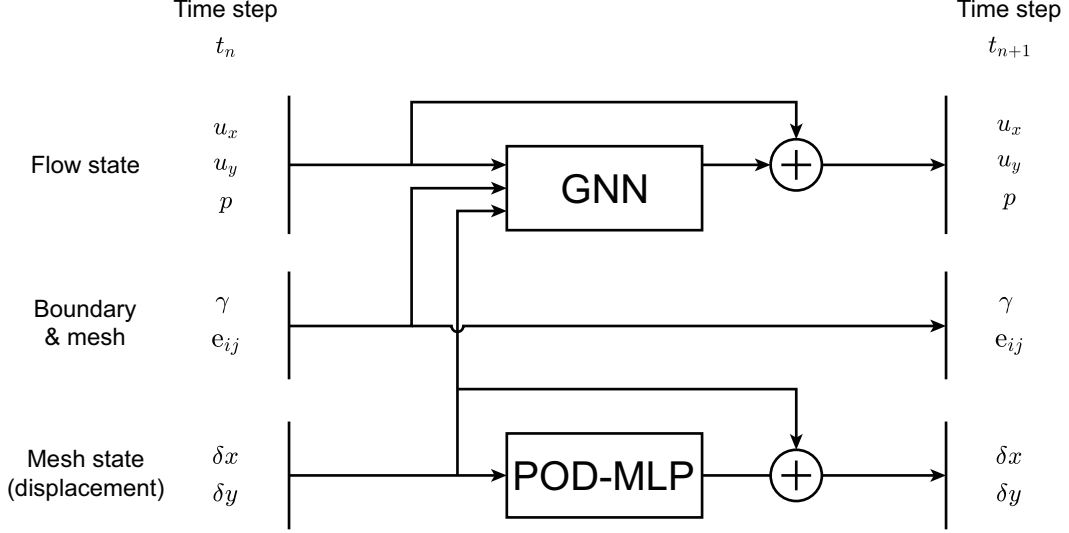


Figure 3: Schematic of the data flow within the proposed quasi-monolithic graph neural network during prediction roll-out. The mesh state at time step t_n is reduced by POD, and then evolved by a multi-layer perceptron to generate the mesh state at time step t_{n+1} . The fluid state at time step t_{n+1} is predicted by a graph neural network, using the whole system state at time step t_n as input. The boundary information and the mesh information are used by the graph neural network in every time step but are not updated. Residual links are adopted following the forward Euler time discretization described in Eq. 5.

step t_n following Eq. 15 and 16, the output from the graph neural network are

$$\hat{v}_{i,out} \approx [u_{x,i}, u_{y,i}, p_i]_{t_{n+1}} - [u_{x,i}, u_{y,i}, p_i]_{t_n}, \quad (17)$$

where $\hat{v}_{i,out}$ denotes the output for node i . The fluid state at time step t_{n+1} is recovered during the temporal roll-out by adding the neural network output to the corresponding entries of the node feature at time step t_n .

3.3 POD-MLP for temporal propagation of mesh

We use a hybrid POD-MLP sub-network to evolve the mesh state. The mesh displacements are first projected to a low dimension using POD, effectively compressing the displacements of all the nodes over time into the evolution of l coefficients. Given the displacement of a mesh containing n_v vertices (nodes) over n_t time steps, the displacements in the x and y directions are stacked to create a matrix X of size $2n_v \times n_t$,

$$X = \begin{bmatrix} \delta x_{1,1} & \delta x_{1,2} & \cdots & \delta x_{1,n_t} \\ \delta x_{2,1} & \delta x_{2,2} & \cdots & \delta x_{2,n_t} \\ \vdots & \vdots & \ddots & \vdots \\ \delta x_{n_v,1} & \delta x_{n_v,2} & \cdots & \delta x_{n_v,n_t} \\ \delta y_{1,1} & \delta y_{1,2} & \cdots & \delta y_{1,n_t} \\ \delta y_{2,1} & \delta y_{2,2} & \cdots & \delta y_{2,n_t} \\ \vdots & \vdots & \ddots & \vdots \\ \delta y_{n_v,1} & \delta y_{n_v,2} & \cdots & \delta y_{n_v,n_t} \end{bmatrix}, \quad (18)$$

and then decomposed and truncated following Eqs. 8 and 9. An MLP is then used for the temporal prediction of these coefficients.

Remark. It is worth mentioning that this idea of a hybrid POD-neural network model has also been used in our previous work [14], where an LSTM [30] network was used along with POD to propagate the mesh location. In this work, we take a further step from that idea, coupling the mesh and fluid prediction during roll-out. We also simplified the network used from an LSTM network to a simple multi-layer perceptron.

The inputs to the MLP are the history of the coefficients corresponding to the first l modes over the last n_h time steps, while the output is the difference between the coefficients at time step t_{n+1} and time step t_n :

$$\text{MLP} \left(c_{t_n}^{(1:l)}, c_{t_{n-1}}^{(1:l)}, \dots, c_{t_{n-n_h+1}}^{(1:l)} \right) = \hat{\delta c}^{(1:l)} \approx c_{t_{n+1}}^{(1:l)} - c_{t_n}^{(1:l)}, \quad (19)$$

in which $\hat{\delta c}^{(1:l)}$ denotes the predicted change of coefficients between time step t_n and time step t_{n+1} . During temporal roll-out, the POD coefficients at time step t_{n+1} are recovered by adding the neural network output to the POD coefficients at time step t_n . The coefficients are then multiplied to the corresponding modes and summed to generate the mesh displacements $(\delta \mathbf{x}, \delta \mathbf{y})_{t_{n+1}}$ for all the nodes. The solid movement is implicitly modelled by the movement of the fluid-solid boundary nodes.

4 Experiments with elastically-mounted cylinder in flowing fluid

In this section, we evaluate the framework constructed in Sec. 3, focusing on its capability to learn the temporal evolution of the FSI system and make accurate temporal roll-out predictions. We consider a representative FSI system of an elastically-mounted cylinder in a laminar flow. In the remaining parts of this section, we will first introduce the generation of the ground truth train and testing data sets, followed by the setup of the model and how it is trained. We then present the metrics used for the evaluation, as well as the results.

4.1 Ground truth data generation

The ground truth data used in this work is the flow around an elastically-mounted cylinder simulated at laminar flow condition. The vibration of a cylinder is governed by the four key non-dimensional parameters, namely mass-ratio (m^*), Reynolds number (Re), reduced velocity (U_r) and critical damping ratio (ζ) defined as

$$m^* = \frac{m^s}{m^f}, \quad Re = \frac{\rho^f U_\infty D}{\mu^f}, \quad U_r = \frac{U_\infty}{f_n D}, \quad \zeta = \frac{c^s}{2\sqrt{k^s m^s}}, \quad (20)$$

where m^s is the mass of the body, c^s and k^s are the damping and stiffness coefficients, respectively for an equivalent mass-spring-damper system of a vibrating structure, U_∞ and D denote the free-stream speed and the diameter of cylinder, respectively. The natural frequency of the body is given by $f_n = (1/2\pi)\sqrt{k^s/m^s}$, the mass of displaced fluid by the structure is $m^f = \rho^f \pi D^2/4$ for a cylinder cross-section. For the current work, we consider the mass ratio $m^* = 10$, the Reynolds number $Re = 200$, the reduced velocity $U_r = 5$ and the damping coefficient $c^s = 0$.

We solve the full-order system (Eqs. 1 and 2) using Petrov-Galerkin finite elements and a semi-discrete time-stepping scheme [28]. The domain and mesh for the ground-truth simulation are plotted in Fig. 4 and 5a. The inlet has a uniform flow $u_x = U_\infty = 1$, $u_y = 0$, the outlet boundary Γ_{out} is traction free, and a slip-wall boundary condition is implemented at top and bottom boundaries Γ_{top} and Γ_{bottom} . The distance between the side walls is $30D$, and the distances to the upstream and the downstream boundaries are $10D$ and $20D$ respectively. The simulation results are validated with the reference values from Li et al. [31]. A total of 2499 continuous steps are sampled from a stable condition with a time step $\Delta t = 0.04$, which is equivalent to the ground truth time step of the full-order simulation.

For the neural network, we use a graph transformed from a coarser mesh (shown in Fig. 5b), which has 2204 nodes and 8728 directed edges. The ground truth ALE mesh movement of the coarser mesh at each time step is calculated from the ground truth displacement $\varphi^m = (\delta \mathbf{x}, \delta \mathbf{y})$ of the cylinder by modeling the mesh as an elastic material in

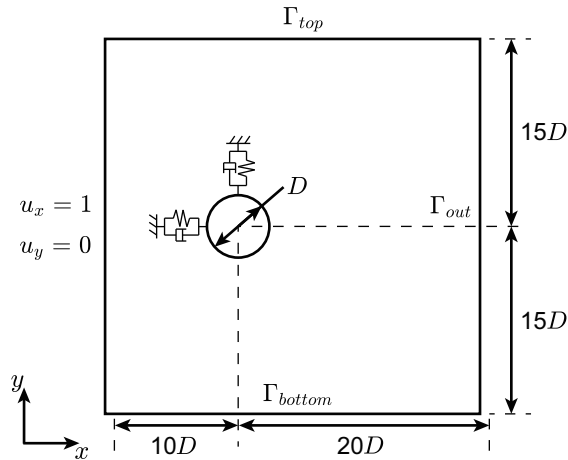


Figure 4: Schematic of an elastically-mounted cylinder for full-order simulation.

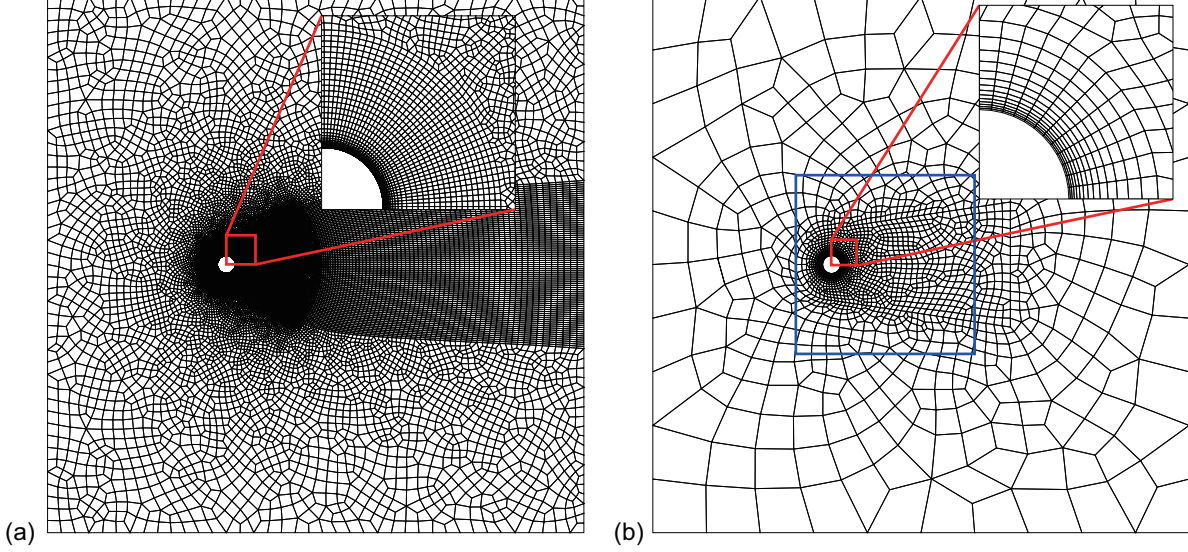


Figure 5: Mesh used for the ground truth simulation and the neural network-based simulation: (a) CFD mesh, (b) graph neural network mesh. Both meshes contain only quadrilateral elements with refinement near the surface of the cylinder and in the wake region. The blue square in (b) marks out the part of the domain being plotted in Fig. 7.

equilibrium, which is given by

$$\nabla \cdot ((1 + k_m)[\nabla \varphi^m + (\nabla \varphi^m)^T + (\nabla \cdot \varphi^m)\mathbf{I}]) = 0, \quad (21)$$

with boundary conditions

$$\varphi^m(t) = \varphi^s(t) - \varphi^s(0) \quad \text{on} \quad \Gamma^{fs}, \quad (22a)$$

$$\varphi^m = 0 \quad \text{on} \quad \partial\Omega^f \setminus \Gamma^{fs}, \quad (22b)$$

where $\partial\Omega^f(0) \setminus \Gamma^{fs}$ denotes the boundary of the fluid domain excluding fluid-solid interface, and k_m is the local element level mesh stiffness parameter [1, 32] which we choose as 0 here for simplicity. The fluid state parameters u_x, u_y, p are then interpolated from the CFD mesh (Fig. 5a) to the coarser mesh (Fig. 5b) via the Clough-Tocher 2D interpolation scheme available in SciPy package [33].

4.2 Train-test split and pre-processing

The interpolated fluid flow data are then attached to the nodes and edges converted from the coarse mesh following Eqs. 15 and 16, and subsequently split into training and testing data sets. Within all 2499 time steps, the first 2061 time steps are used for training purposes, and the rest are used for testing purposes.

For the fluid state prediction, we construct two sets of training data. In the one-step prediction training set, the input nodes $v_i|_{t_n}$ and edges e_{ij} corresponds to the output nodes $[u_{x,i}, u_{y,i}, p_i]_{t_{n+1}} - [u_{x,i}, u_{y,i}, p_i]_{t_n}$. In the five-step roll-out prediction training set, the input nodes $v_i|_{t_n}$ and edges e_{ij} corresponds to output nodes $[u_{x,i}, u_{y,i}, p_i]_{t_{n+5}} - [u_{x,i}, u_{y,i}, p_i]_{t_{n+4}}$. The input and output nodes and edges are then normalized to zero mean and unit variance, respectively.

For the mesh displacement prediction, we only use the one-step prediction data for training, in which each input $\begin{bmatrix} c_{t_n}^{(1:l)}, c_{t_{n-1}}^{(1:l)}, \dots, c_{t_{n-n_h+1}}^{(1:l)} \end{bmatrix}$ corresponds to an output $\begin{bmatrix} c_{t_{n+1}}^{(1:l)} - c_{t_n}^{(1:l)} \end{bmatrix}$, with the number of history steps chosen as $n_h = 3$. The proper orthogonal decomposition is performed on the centred mesh displacement data set over all the 2061 time steps used for training. The coefficients are normalized to zero mean and unit variance before constructing the inputs and outputs, which are normalized again afterwards. We only use $l = 2$ modes for the reduced-order model, as the mesh displacement matrix is inherently rank-2.

The network is expected to generate accurate roll-out predictions, and therefore the test set is designed such that the neural network roll-out can start from any time step within the test set. At each time step within the data set, the data available are the inputs to the fluid state prediction $v_i|_{t_n}$ and e_{ij} , as well as the inputs to the mesh displacement

Table 1: Training and testing data sets

	Name	Inputs	Output	Total samples
Training sets	One step, fluid	$\mathbf{v}_i _{t_n}, \mathbf{e}_{ij}$	$[u_{x,i}, u_{y,i}, p_i]_{t_{n+1}} - [u_{x,i}, u_{y,i}, p_i]_{t_n}$	2048
	5 steps, fluid		$[u_{x,i}, u_{y,i}, p_i]_{t_{n+5}} - [u_{x,i}, u_{y,i}, p_i]_{t_{n+4}}$	
	One step, mesh	$[c_{t_n}^{(1:2)}, c_{t_{n-1}}^{(1:2)}, c_{t_{n-2}}^{(1:2)}]$	$[c_{t_{n+1}}^{(1:2)}] - [c_{t_n}^{(1:2)}]$	
Testing sets	Roll-out, fluid	$\mathbf{v}_i _{t_n}, \mathbf{e}_{ij}$	N/A	435
	Roll-out, mesh	$[c_{t_n}^{(1:2)}, c_{t_{n-1}}^{(1:2)}, c_{t_{n-2}}^{(1:2)}]$	N/A	

Table 2: Neural network training details.

Sub-network (total params; optimizer)	Stage	Training set	Batch size	Epochs	Starting learning rate	Learning rate decay per epoch
Fluid prediction (2.33 M; Adam)	1	One step, fluid	4	6	10^{-6}	2.152
	2			50	10^{-4}	1
	3			100	10^{-4}	0.955
	4			50	10^{-6}	1
	5			5 steps, fluid	2	50
Mesh prediction (267 K; AdamW)	1	One step, mesh	512	200	10^{-4}	0.98

prediction $[c_{t_n}^{(1:l)}, c_{t_{n-1}}^{(1:l)}, \dots, c_{t_{n-n_h+1}}^{(1:l)}]$. These data are normalized using the mean and variance statistics calculated from the training data sets.

Table 1 summarizes the data sets.

4.3 Model and training details

With the training and testing data sets available, we proceed to set up and train the model. The implementation is completed with the PyTorch package [34]. For the graph neural network used in the fluid state prediction, the encoders, decoder, and the node and edge processors for each message-passing layer are all selected to be MLPs with two hidden layers and Gaussian Error Linear Unit activation function [35]. The layer widths of all these MLPs are fixed at 128 following Pfaff et al. [20]. The weights and biases are initialized with PyTorch default setting. We tested over different numbers of message-passing layers since we use a quadrilateral mesh rather than the triangular mesh in most existing works, and it seems that 15 message-passing layers are still a reasonable choice to achieve the balance between accuracy and computational cost. Layer normalization [36] is utilized after all encoders as well as all node and edge processors to facilitate convergence. The graph message-passing is implemented using the gather-scatter scheme following the practice in PyTorch Geometric package [37].

For the MLP used for the mesh displacement prediction, we use two hidden layers (i.e., $n_l = 3$) with a layer width of 512. A sinusoidal activation function [38] and the corresponding initialization scheme is adopted. With history size $n_h = 3$, the input size is six, and the output size is 2.

The two sub-networks are trained separately on a single Nvidia RTX 3090 GPU with a central processing unit (CPU) being AMD Ryzen 9 5900 @ 3 GHz \times 12 cores. The fluid state prediction sub-network is trained with an Adam optimizer [39] for a total of 206 epochs, divided into five stages listed in table 2. The mesh displacement prediction sub-network is trained for 200 epochs with batch size 512. An AdamW [40] optimizer is used with a learning rate starting at 10^{-4} and an exponential learning rate decay of 0.98 per epoch. For both networks, we use a mean-square error loss normalized on each batch as given by:

$$\mathcal{L} = \frac{\|\psi - \hat{\psi}\|_2^2}{\|\psi\|_2^2}, \quad (23)$$

where ψ denotes the ground truth output for the batch, and $\hat{\psi}$ denotes the predicted output from the neural network. Note that this loss is not the normalized mean square loss, as we sum over the numerator and denominator before the division under the consideration of numerical stability.

Table 3: Time required per prediction roll-out step

Component	Time per step
Total	≈ 21.4 ms
Fluid prediction sub-network	≈ 12.4 ms
Mesh prediction sub-network	≈ 0.2 ms
Other overhead	≈ 8.8 ms

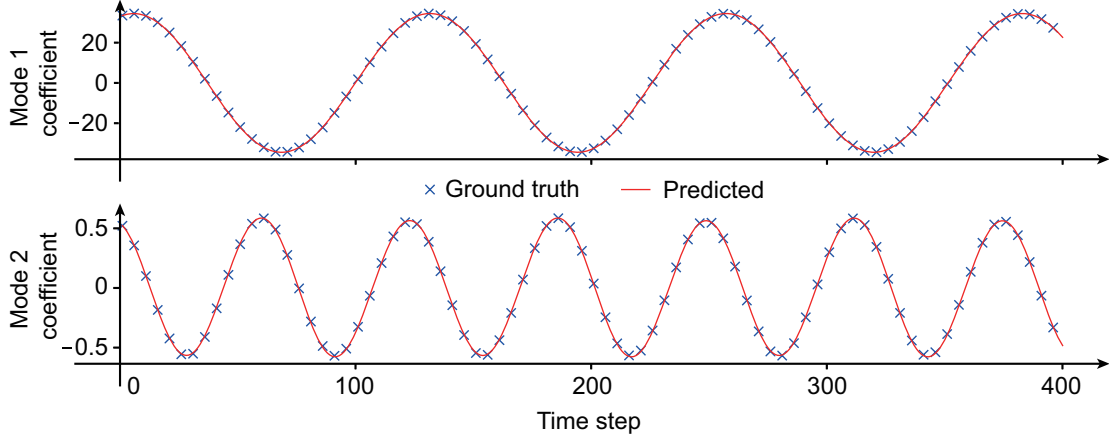


Figure 6: Predicted vs. ground truth mode coefficients for the mesh displacement during prediction roll-out over 400 steps, starting from the first time step within the test data set.

4.4 Evaluation metrics

After training, the framework is evaluated on the testing data set to evaluate its performance in producing temporal roll-out predictions. We consider several metrics to facilitate the evaluation. Qualitatively, we plot out the predicted pressure fields at different time steps during the prediction roll-out, and compare them with the ground truth. Quantitatively, we use the coefficient of determination R^2 to evaluate the accuracy of predictions for the system states, which can be calculated given the system state parameter s and its prediction \hat{s}

$$R^2 = 1 - \frac{\|s - \hat{s}\|_2^2}{\|s - \bar{s}\|_2^2}, \quad (24)$$

where $\bar{\cdot}$ denotes the calculation of mean. A coefficient of determination close to 1 means that the error of the prediction is low. In addition, we also extract the lift coefficient C_l and drag coefficient C_d on the cylinder from the predicted system state. The calculation is performed by integrating the Cauchy stress tensor σ^f (defined in Eq. 3) from the first layer of element away from the cylinder,

$$C_l = \frac{1}{\frac{1}{2}\rho^f(U_\infty)^2 D} \int_{\Gamma^{fs}} (\sigma^f \cdot \mathbf{n}) \cdot \mathbf{n}_y d\Gamma, \quad (25a)$$

$$C_d = \frac{1}{\frac{1}{2}\rho^f(U_\infty)^2 D} \int_{\Gamma^{fs}} (\sigma^f \cdot \mathbf{n}) \cdot \mathbf{n}_x d\Gamma, \quad (25b)$$

where $U_\infty = 1$ is the inlet velocity, and the characteristic length D is the diameter of the cylinder in this work. It should be noted that this way of calculation is different from our previous work [14], as only pressure lift and drag coefficients were considered in that work, but the contribution from viscous forces were not calculated. It is also different from works like [15], as they did not calculate the lift and drag coefficients from the predicted flow and mesh states, but rather model and evolve them separately.

4.5 Results

In this subsection, we present the results when evaluating the framework on the test data set, using the metrics listed in Sec. 4.4. Table 3 summarizes the approximate computational time needed for each prediction roll-out step when running

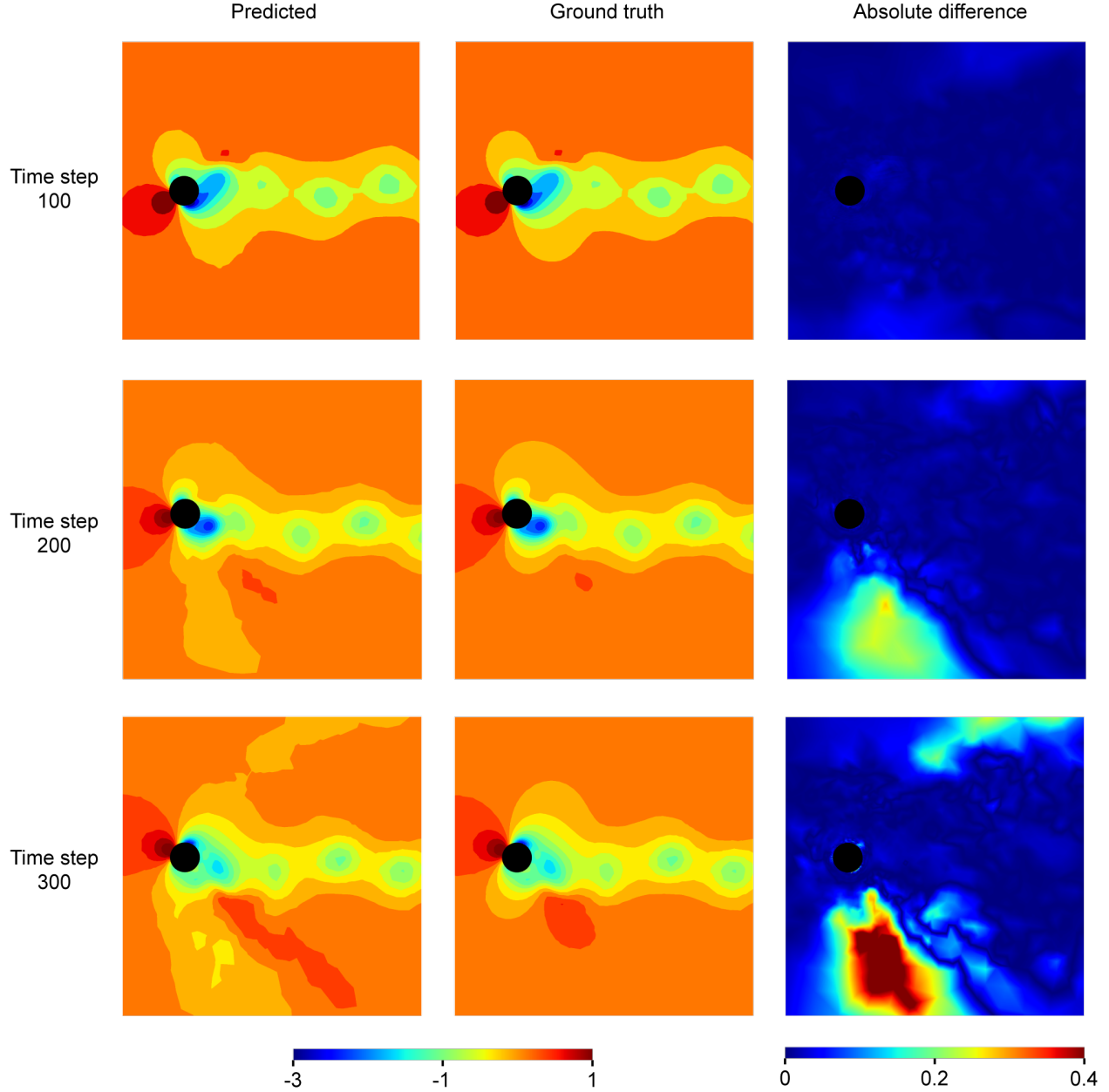


Figure 7: Predicted vs. ground truth normalized pressure field $p^* = 2p/\rho^f U_\infty^2$ near the cylinder, at 100, 200, and 300 steps during prediction roll-out. The region plotted is marked out by a blue square in Fig. 5b.

on an Nvidia RTX 2060 GPU with AMD Ryzen 7 4800H CPU @ 2.90 GHz \times 8 cores. Approximately 2.1 GB GPU memory is required for the roll-out during the tests, including the model parameters, the buffers and other overhead.

The roll-out prediction of mesh POD coefficients over 400 time steps using the mesh prediction sub-network, starting from the first time step within the test data set (step 2064 within all the 2499 time steps), is plotted in Fig. 6. It is clear that the mesh prediction sub-network produces stable and accurate predictions of mesh displacements over time. We then assemble it with the fluid prediction sub-network for the roll-out predictions of the whole system state, following the data flow shown in Fig. 3.

System state prediction. Starting from the first time step within the test data set, we predict the system states over the next 300 time steps. Figure 7 shows the predicted versus the ground truth normalized pressure $p^* = 2p/\rho^f U_\infty^2$ near the cylinder at steps 100, 200 and 300. The plotted area is marked by a blue square in Fig. 5b. For the purpose of

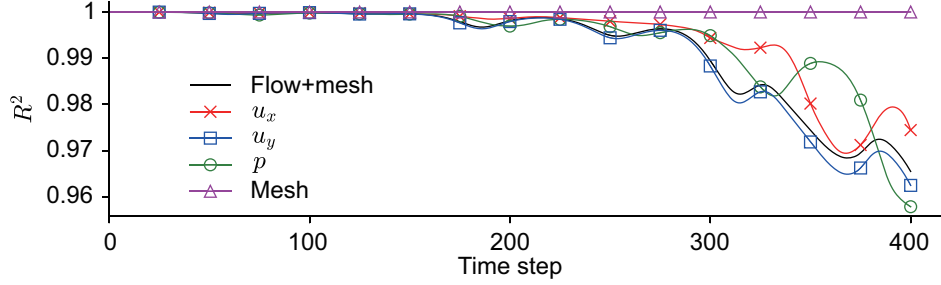


Figure 8: Coefficient of determinations of the system state and its components over 400 prediction roll-out steps.

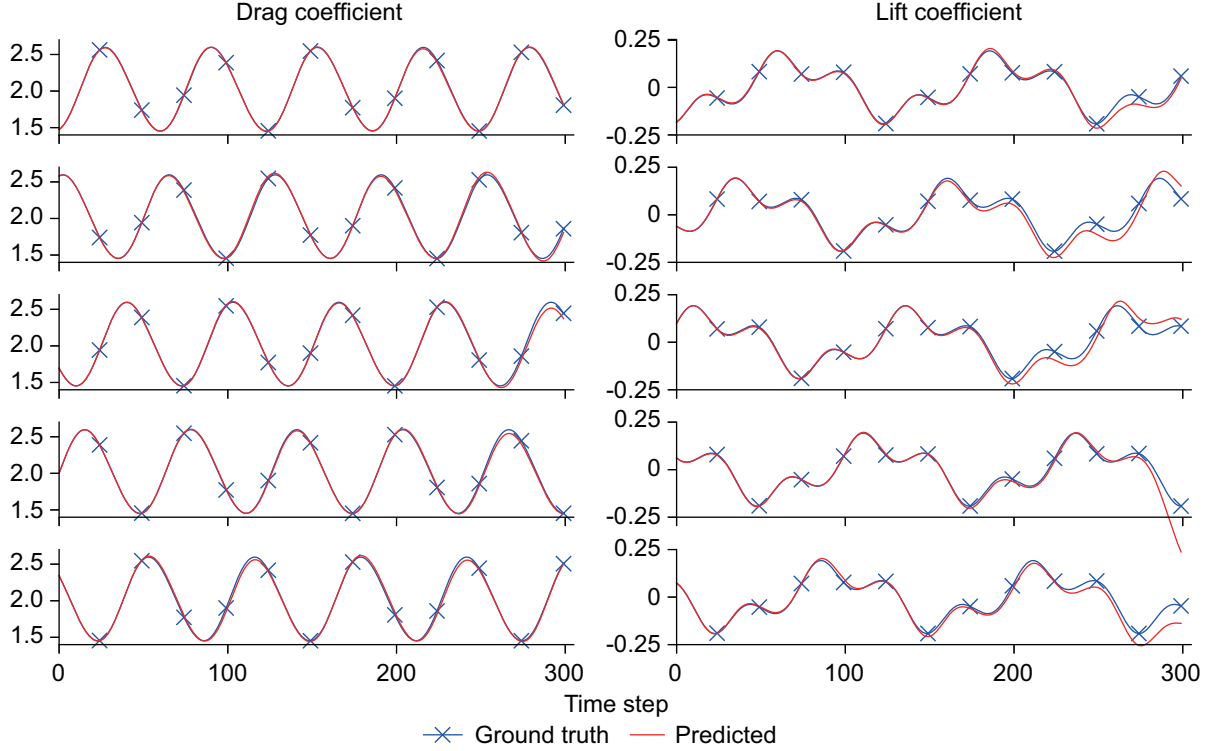


Figure 9: Predicted vs. ground truth lift and drag coefficients during prediction roll-out over 300 steps, starting from different time steps within the test set. From top to bottom, time steps include 1, 26, 51, 76, 101 within the test set.

plotting, the predicted field is projected onto a 512×512 uniform Cartesian grid using a linear interpolation scheme available in the SciPy package [33]. The cylinder is plotted by linking the predicted locations of its boundary nodes. The model is able to produce visually accurate prediction results at time step 100. At 200 and 300 steps, the error starts to become more pronounced visually in the regions below and above the cylinder, where the mesh (cf. Fig. 5) is relatively sparse. This is a result of accumulated errors over the roll-out time steps. Nevertheless, the predictions in the wake region, where the mesh resolution is relatively high, remain visually accurate over all 300 predicted steps. We also plot the coefficient of determination for the predicted system state, as well as its components, over 400 time steps in Fig. 8. Quantitatively, the coefficients of determination for the system state, as well as its components, are very close to 1 in the first 150 steps, indicating accurate predictions of the temporal evolution of the system. After that, the error starts to accumulate slowly for the fluid state predictions, while mesh state predictions remain accurate.

Lift and drag coefficients prediction. In addition to calculating the coefficient of determinations of the fluid and mesh state parameters, we also quantify the error of the predicted system state by calculating the lift and drag coefficients over time following Eq. 25. It should be emphasized again that we are directly integrating the lift and drag from the predicted system states, without any interpolation or smoothing procedures. Starting from different time steps within the testing data set, we plot out the predicted and ground truth lift and drag coefficients over 300 steps in Fig. 9.

Accurate predictions of lift and drag coefficients can be extracted from the predicted flow field accurate over the first 200 steps for all these cases. After that, error starts to occur for the predicted lift coefficient, while the predicted drag coefficient stays accurate.

5 Conclusions

We presented a quasi-monolithic graph neural network-based framework for data-driven reduced-order modeling of fluid-structure interaction systems. Adopting the arbitrary Lagrangian-Eulerian formulation, the proposed framework relies on a multi-layer perceptron for predicting POD coefficients to evolve mesh displacements, and a graph neural network for predicting fluid states from the current system state. The framework is applied to the flow around an elastically mounted cylinder at Reynolds number $Re = 200$. Starting from a given system state, the model can produce accurate predictions of the system state over 150 time steps, and the error only starts to accumulate slowly after that in poorly-resolved regions. Accurate fluid and mesh state predictions on a non-uniform mesh, refined near the surface of the cylinder, enable the direct and accurate extraction of lift and drag forces over 200 time steps via the integration of the Cauchy stress tensor on the cylinder surface, which is difficult with existing convolution-based works. It should be noted that the framework proposed in this work applies to fluid-structure interaction systems with rigid solid bodies. In our future work, we plan to extend the application to fluid-structure interaction systems with deformable elastic structures.

Acknowledgments

The authors would like to acknowledge the Natural Sciences and Engineering Research Council of Canada (NSERC) and Seaspan Shipyards for the funding. This research was supported in part through computational resources and services provided by Advanced Research Computing at the University of British Columbia.

References

- [1] Rajeev K Jaiman and Vaibhav Joshi. *Computational Mechanics of Fluid-Structure Interaction*. Springer, 2022.
- [2] John L Lumley. The structure of inhomogeneous turbulent flows. In *Atmospheric Turbulence & Wave Propagation*, 1967.
- [3] Lawrence Sirovich. Turbulence and the dynamics of coherent structures. part I. coherent structures. *Quarterly of Applied Mathematics*, 45(3):561–571, 1987.
- [4] Peter J Schmid. Dynamic mode decomposition of numerical and experimental data. *Journal of fluid mechanics*, 656:5–28, 2010.
- [5] Aaron Towne, Oliver T Schmidt, and Tim Colonius. Spectral proper orthogonal decomposition and its relationship to dynamic mode decomposition and resolvent analysis. *Journal of Fluid Mechanics*, 847:821–867, 2018.
- [6] Oliver T Schmidt and Peter J Schmid. A conditional space–time pod formalism for intermittent and rare events: example of acoustic bursts in turbulent jets. *Journal of Fluid Mechanics*, 867, 2019.
- [7] Hao Zhang, Clarence W Rowley, Eric A Deem, and Louis N Cattafesta. Online dynamic mode decomposition for time-varying systems. *SIAM Journal on Applied Dynamical Systems*, 18(3):1586–1609, 2019.
- [8] Geoffrey E Hinton and Ruslan R Salakhutdinov. Reducing the dimensionality of data with neural networks. *science*, 313(5786):504–507, 2006.
- [9] Francisco J Gonzalez and Maciej Balajewicz. Deep convolutional recurrent autoencoders for learning low-dimensional feature dynamics of fluid systems. *arXiv preprint arXiv:1808.01346*, 2018.
- [10] Nils Thuerey, Konstantin Weißenow, Lukas Prantl, and Xiangyu Hu. Deep learning methods for reynolds-averaged navier–stokes simulations of airfoil flows. *AIAA Journal*, 58(1):25–36, 2020.
- [11] Sandeep R Bukka, Rachit Gupta, Allan R Magee, and Rajeev K Jaiman. Assessment of unsteady flow predictions using hybrid deep learning based reduced-order models. *Physics of Fluids*, 33(1):013601, 2021.
- [12] Pranshu Pant, Ruchit Doshi, Pranav Bahl, and Amir Barati Farimani. Deep learning for reduced order modelling and efficient temporal evolution of fluid simulations. *Physics of Fluids*, 33(10):107101, 2021.
- [13] Rachit Gupta and Rajeev K Jaiman. Three-dimensional deep learning-based reduced order model for unsteady flow dynamics with variable reynolds number. *Physics of Fluids*, 34(3):033612, 2022.

- [14] Rachit Gupta and Rajeev K Jaiman. A hybrid partitioned deep learning methodology for moving interface and fluid–structure interaction. *Computers & Fluids*, 233:105239, 2022.
- [15] Xinshuai Zhang, Tingwei Ji, Fangfang Xie, Changdong Zheng, and Yao Zheng. Data-driven nonlinear reduced-order modeling of unsteady fluid–structure interactions. *Physics of Fluids*, 34(5):053608, 2022.
- [16] Wrik Mallik, Rajeev K Jaiman, and Jasmin Jelovica. Predicting transmission loss in underwater acoustics using convolutional recurrent autoencoder network. *The Journal of the Acoustical Society of America*, 152(3):1627–1638, 2022.
- [17] Zheng Wang, Dunhui Xiao, Fangxin Fang, Rajesh Govindan, Christopher C Pain, and Yike Guo. Model identification of reduced order fluid dynamics systems using deep learning. *International Journal for Numerical Methods in Fluids*, 86(4):255–268, 2018.
- [18] Sandeep B Reddy, Allan R Magee, Rajeev K Jaiman, J Liu, W Xu, A Choudhary, and A A Hussain. Reduced order model for unsteady fluid flows via recurrent neural networks. In *International Conference on Offshore Mechanics and Arctic Engineering*, volume 58776, page V002T08A007. American Society of Mechanical Engineers, 2019.
- [19] Li-Wei Chen and Nils Thuerey. Towards high-accuracy deep learning inference of compressible turbulent flows over aerofoils. *arXiv preprint arXiv:2109.02183*, 2021.
- [20] Tobias Pfaff, Meire Fortunato, Alvaro Sanchez-Gonzalez, and Peter W Battaglia. Learning mesh-based simulation with graph networks. *arXiv preprint arXiv:2010.03409*, 2020.
- [21] Mario Lino, Stathi Fotiadis, Anil A Bharath, and Chris D Cantwell. Multi-scale rotation-equivariant graph neural networks for unsteady eulerian fluid dynamics. *Physics of Fluids*, 34(8):087110, 2022.
- [22] Jiayang Xu, Aniruddhe Pradhan, and Karthikeyan Duraisamy. Conditionally parameterized, discretization-aware neural networks for mesh-based modeling of physical systems. *Advances in Neural Information Processing Systems*, 34:1634–1645, 2021.
- [23] Filipe De Avila Belbute-Peres, Thomas Economon, and Zico Kolter. Combining differentiable pde solvers and graph neural networks for fluid flow prediction. In *international conference on machine learning*, pages 2402–2411. PMLR, 2020.
- [24] Xiaodong He, Yinan Wang, and Juan Li. Flow completion network: Inferring the fluid dynamics from incomplete flow information using graph neural networks. *arXiv preprint arXiv:2205.04739*, 2022.
- [25] Leon Migus, Yuan Yin, Jocelyn Ahmed Mazari, and Patrick Gallinari. Multi-scale physical representations for approximating pde solutions with graph neural operators. *arXiv preprint arXiv:2206.14687*, 2022.
- [26] Han Gao, Matthew J Zahr, and Jian-Xun Wang. Physics-informed graph neural galerkin networks: A unified framework for solving pde-governed forward and inverse problems. *Computer Methods in Applied Mechanics and Engineering*, 390:114502, 2022.
- [27] Yunzhu Li, Jiajun Wu, Russ Tedrake, Joshua B Tenenbaum, and Antonio Torralba. Learning particle dynamics for manipulating rigid bodies, deformable objects, and fluids. *arXiv preprint arXiv:1810.01566*, 2018.
- [28] Rajeev K Jaiman, M Z Guan, and Tharindu P Miyanawala. Partitioned iterative and dynamic subgrid-scale methods for freely vibrating square-section structures at subcritical reynolds number. *Computers & Fluids*, 133:68–89, 2016.
- [29] Peter W Battaglia, Jessica B Hamrick, Victor Bapst, Alvaro Sanchez-Gonzalez, Vinicius Zambaldi, Mateusz Malinowski, Andrea Tacchetti, David Raposo, Adam Santoro, Ryan Faulkner, et al. Relational inductive biases, deep learning, and graph networks. *arXiv preprint arXiv:1806.01261*, 2018.
- [30] Sepp Hochreiter and Jürgen Schmidhuber. Long short-term memory. *Neural computation*, 9(8):1735–1780, 1997.
- [31] Zhong Li, Weigang Yao, Kun Yang, Rajeev K Jaiman, and Boo Cheong Khoo. On the vortex-induced oscillations of a freely vibrating cylinder in the vicinity of a stationary plane wall. *Journal of Fluids and Structures*, 65:495–526, 2016.
- [32] Arif Masud and Thomas JR Hughes. A space-time galerkin/least-squares finite element formulation of the navier-stokes equations for moving domain problems. *Computer methods in applied mechanics and engineering*, 146(1-2):91–126, 1997.
- [33] Pauli Virtanen, Ralf Gommers, Travis E Oliphant, Matt Haberland, Tyler Reddy, David Cournapeau, Evgeni Burovski, Pearu Peterson, Warren Weckesser, Jonathan Bright, Stéfan J van der Walt, Matthew Brett, Joshua Wilson, K Jarrod Millman, Nikolay Mayorov, Andrew R J Nelson, Eric Jones, Robert Kern, Eric Larson, C J Carey, İlhan Polat, Yu Feng, Eric W Moore, Jake VanderPlas, Denis Laxalde, Josef Perktold, Robert Cimrman, Ian Henriksen, E A Quintero, Charles R Harris, Anne M Archibald, Antônio H Ribeiro, Fabian Pedregosa, Paul van

- Mulbregt, and SciPy 1.0 Contributors. SciPy 1.0: Fundamental Algorithms for Scientific Computing in Python. *Nature Methods*, 17:261–272, 2020.
- [34] Adam Paszke, Sam Gross, Francisco Massa, Adam Lerer, James Bradbury, Gregory Chanan, Trevor Killeen, Zeming Lin, Natalia Gimelshein, Luca Antiga, et al. Pytorch: An imperative style, high-performance deep learning library. *Advances in neural information processing systems*, 32, 2019.
 - [35] Dan Hendrycks and Kevin Gimpel. Gaussian error linear units (gelus). *arXiv preprint arXiv:1606.08415*, 2016.
 - [36] Jimmy Lei Ba, Jamie Ryan Kiros, and Geoffrey E Hinton. Layer normalization. *arXiv preprint arXiv:1607.06450*, 2016.
 - [37] Matthias Fey and Jan E Lenssen. Fast graph representation learning with PyTorch Geometric. In *ICLR Workshop on Representation Learning on Graphs and Manifolds*, 2019.
 - [38] Vincent Sitzmann, Julien Martel, Alexander Bergman, David Lindell, and Gordon Wetzstein. Implicit neural representations with periodic activation functions. *Advances in Neural Information Processing Systems*, 33:7462–7473, 2020.
 - [39] Diederik P Kingma and Jimmy Ba. Adam: A method for stochastic optimization. *arXiv preprint arXiv:1412.6980*, 2014.
 - [40] Ilya Loshchilov and Frank Hutter. Decoupled weight decay regularization. *arXiv preprint arXiv:1711.05101*, 2017.